

Island formation and dynamics of gold clusters on amorphous carbon films

Matthias Wanner,¹ Ralph Werner,² Günter Schneider,² and Dagmar Gerthsen¹

¹*Laboratorium für Elektronenmikroskopie, Universität Karlsruhe, 76128 Karlsruhe*

²*Institut für Theorie der Kondensierten Materie, Universität Karlsruhe, 76128 Karlsruhe*

(Dated: December 2, 2024)

Samples of Au clusters deposited by laser ablation on an amorphous-carbon substrate are investigated. After a few months storage at room temperature the initially statistically distributed clusters are found to be collected in agglomerates consisting of larger clusters embedded in an Au film typically covering areas of size $25 \times 70 \text{ nm}^2$. The Au film is determined to be probably 4 to 8 monolayers but at most 7 nm thick. Evidence is found that a number of clusters consisting of less than 50 atoms are pinned at intrusions of the substrate. These results were derived using high resolution transmission electron microscopy and off-axis holography measurements to characterize the agglomerates as well as the substrate. Monte Carlo simulations were performed to model the film formation process. To this end the substrate-Au interaction was determined using density functional calculations (GGA) while the Au-Au interaction was modeled with effective many body Gupta potentials. The film formation can be understood as diffusion and fusion of clusters of intermediate ($50 < N < 300$ atoms) size. Larger clusters are more stable at room temperature and remain adsorbed on the Au film.

I. INTRODUCTION

The dynamic behavior of clusters deposited on a substrate has been studied for several decades.^{1,2,3,4,5,6} A continuously growing number of potential applications in electronics^{7,8} and catalysis^{9,10} demands defined arrays of nanoparticles. However, such arrays tend to minimize their energy by minimizing the total surface via the growth of larger particles at the expense of smaller ones.¹ An example for such a process is Ostwald ripening, where the larger cohesive energy in larger particles leads to matter transport away from small particles in the presence of a finite partial pressure of the constituent in the environment surrounding the clusters.^{11,12} Therefore, investigations concerning the stability^{13,14} of deposited nanoparticles are of considerable interest with respect to potential nano-technological applications.

Moreover, the thermodynamic^{15,16} and chemical¹⁷ properties of small metal clusters themselves have enjoyed a large interest over the past years. Their properties differ from those of the bulk material raising the fundamental question about the statistical mechanics of finite systems.¹⁸ Since the presence of a substrate alters these properties^{9,19} detailed investigations of the substrate-adsorbate interaction²⁰ are required.

In this paper we present results from transmission electron microscopy (TEM) investigations^{21,22} concerning the time- and temperature-dependent behavior of Au clusters deposited by laser ablation technique on amorphous-carbon (a-C) films. The reasons to choose an amorphous substrate are threefold. Firstly, the non-crystalline structure of the substrate allows for the visualization of the crystal structure of the adsorbed clusters in high resolution TEM (HRTEM) experiments. Secondly, amorphous carbon is mechanically much more stable than highly oriented pyrolytic graphite (HOPG) and consequently much more suited for technical applications. Thirdly, as opposed to the conductor HOPG, amorphous carbon is semi-conducting^{23,24} and as such is

expected to be less influential on the electronic properties of the adsorbate. Furthermore, our observations were made on samples that were stored under normal atmosphere for several months enhancing their relevance for possible technical applications.

The central observation reported in this paper is the formation of islands on a time scale of several months after the deposition of the Au adsorbate. Typical TEM images of the samples are shown in Fig. 1. Panel (a) is a sample one day after its preparation. The inset shows the size distribution of the clusters. Clusters smaller than 1 nm in diameter cannot be resolved unambiguously because of their low contrast on the amorphous substrate. Panel (b) shows a typical island formed after the sample has been aged for 4 months.

While the formation of small islands on short time scales has been observed previously for larger size-selected clusters for Co on microgrid substrates,⁴ for Au on amorphous carbon,⁵ as well as for Ag on graphite,⁶ the new features here are dark areas typically covering $25 \times 70 \text{ nm}^2$ underlying the larger clusters. As described in this paper in detail we were able to identify these areas as islands consisting of Au films of roughly 4 to 8 monolayers thickness with immersed larger Au clusters. The Au films show areas of crystalline structure with essentially two different lattice plane orientations as shown in the circled areas in Fig. 1(c). A close analysis of the properties of the Au films including a holographic determination of its thickness is given in Sec. IV. We arrive at the conclusion that the islands are formed by coalescing small clusters with diameters of $< 2 \text{ nm}$.

The island formation was observed “by accident” on the batch of stored samples. Consequently no monitoring of the dynamics of the formation of the islands—as desirable—was done. Awaiting the preparation of new samples, which are needed for the observation of the formation process, the present paper aims to give a state-of-the-art analysis of the system at hand. Based on these findings the time-analysis will be performed once new

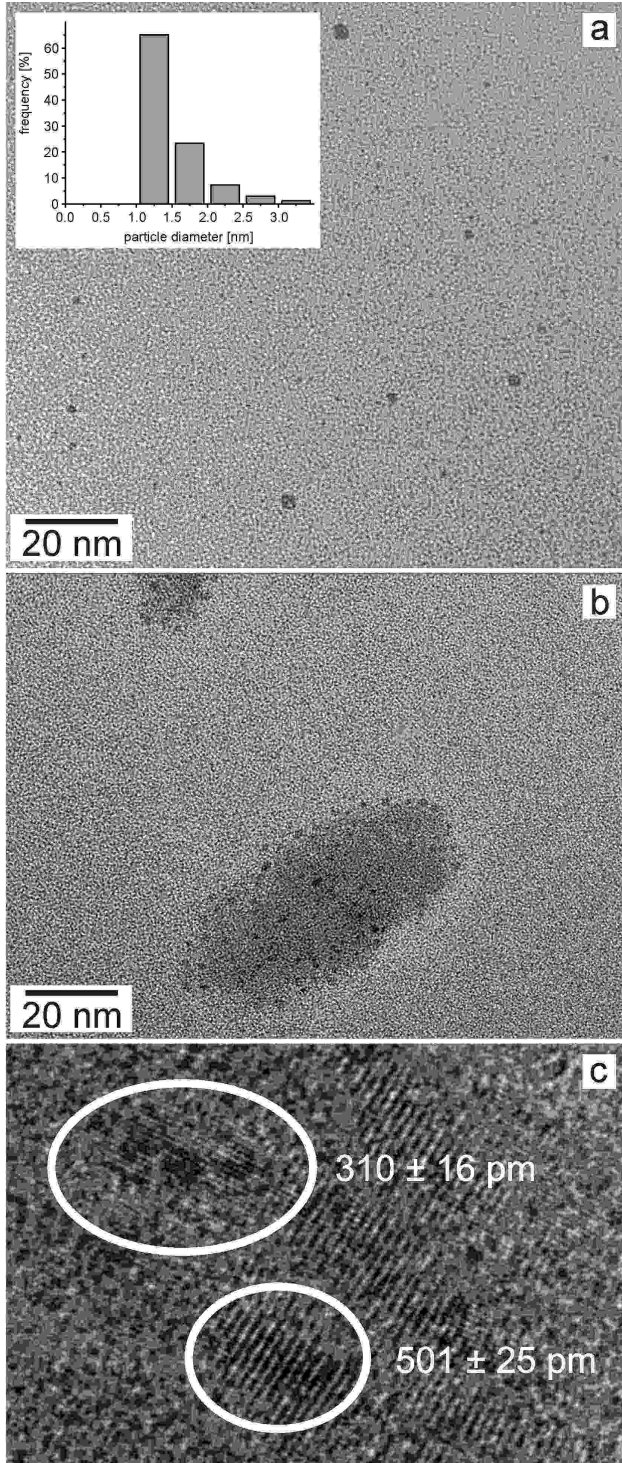


FIG. 1: TEM images of Au clusters deposited on an a-C substrate by laser ablation (3000 shots): (a) sample one day after its preparation. The inset shows the histogram of the size-distribution of the clusters. Clusters smaller than 1nm in diameter cannot be resolved unambiguously within the TEM images. (b) Typical island of higher contrast formed on a sample four months after its preparation. (c) Detail of the island displayed in panel (b). The areas circled show regions exhibiting crystalline structures with differently spaced lattice planes.

samples are available.

Outline of the paper

In Sec. II we describe the experimental [sample preparation and TEM] as well as theoretical [density functional theory (DFT) and Monte-Carlo (MC) simulations] methods applied.

Since the main trade-off of the amorphous substrate is its less well defined surface we devote Sec. III to develop a model of the carbon film that is consistent with the experimental observations. To this end holographic images of the substrate film are analyzed (Sec. III A). First principle DFT calculations allow for the determination of the substrate-Au interaction (Sec. III B).

In Sec. IV the observed islands are analyzed in detail. Their thickness is determined holographically (Sec. IV B) and their stability tested in a heating experiment (Sec. IV D).

In Sec. V the formation of the islands and the shape of the Au clusters on their surface is modeled with MC simulations followed by the conclusion Sec. VI.

II. METHODS

A. Substrate and sample preparation

The commercial a-C substrate films were produced by evaporation in a carbon arc by Arizona Carbon Foils and distributed by Plano GmbH as type S160. The films are mounted on a 200 nm mesh Cu grid for support. The film thickness is given by the manufacturer as $d_{\text{subs}} = 10 - 12.5$ nm with a density of $\rho_{\text{subs}} \approx 2.0$ g/cm³ corresponding to a mass of $2 - 2.5\mu\text{g}/\text{cm}^2$. The density of the substrate is closer to that of graphite ($\rho_{\text{graph}} = 2.267$ g/cm³) than to that of diamond ($\rho_{\text{dia}} = 3.515$ g/cm³) suggesting a structure that contains regions with trivalent coordination.²³ The similarities in the electronic structure between a-C and graphite are supported by electron energy loss spectroscopy (EELS) measurements,²⁴ which show spectra that differ significantly from those of diamond. Amorphous-carbon films produced with similar methods and of similar density have been found to be semi-conducting.^{23,25}

Note that, since $\rho_{\text{subs}} < \rho_{\text{graph}}$ and since in the amorphous material some tetravalent C with higher local density must be present, there must exist areas with very low density or even voids for compensation. This assumption is supported by the results presented in Sec. III.

The Au clusters were collected from the primary beam of a laser vaporization cluster source, which has been described elsewhere in detail.^{26,27} In brief, the laser vaporization cluster source is a variant of the Smalley-deHeer-type^{28,29} setup optimized by Heiz³⁰ for high yield. The source is equipped with a rotating gold disc target with a diameter of 50 mm which is sealed with a Teflon gasket against the source block. A pulsed laser (Neodym-YAG,

Continuum, 532 nm, 30 Hz repetition rate) is focused through a nozzle onto the target. A pulsed valve (General Valve, 5 bar backing pressure of He) which is synchronized with the laser quenches the evaporated atoms into clusters which expand through the nozzle and a skimmer into an oil diffusion pumped vacuum chamber at 10^{-5} mbar. Au clusters (and atoms) are deposited without further mass selection onto a TEM grid placed in the primary beam in a distance of about 40 cm from the nozzle.

The size distribution of the Au particles is shown in the inset of Fig. 1(a). Since the only directed acceleration of the clusters is the expansion into the vacuum of the cluster source the impact energy can be considered small enough to avoid intercalation of adsorbate and substrate.

B. Transmission electron microscopy

The TEM was carried out with a Philips CM200 FEG/ST electron microscope at an energy of 200 keV equipped with a Noran Ge detector system for energy-dispersive X-ray analysis (EDX). A Gatan 652 Double Tilt Heating Holder operated by a Gatan 901 SmartSet Hot Stage Controller was used to perform the *in situ* annealing experiments.

Transmission electron holography was carried out using a Möllenstedt biprism installed in the selected-area aperture holder of the microscope. The electrostatic potential of the biprism wire was close to 150 V. The images recorded were analyzed using the phase shift of the (000)-beam of the first hologram sideband. Data analysis was performed using the DALI program package,³¹ which was extended for the reconstruction of holograms. The details of the reconstruction of holograms are outlined by Lichte and Lehmann.²²

Figure 2 shows the three-dimensional visualization of the phase shift³² with respect to the vacuum $\Delta\phi$ observed on a $28.2 \times 28.2 \text{ nm}^2$ surface segment of a typical sample. In the far right corner a part of an island as shown in Fig. 1(b) is visible. In the front left corner the linear decrease of the thickness of the substrate near the substrate edge is visible. All holographic images were taken at substrate edges in order to include a section of the vacuum for calibration.^{21,22} A closer analysis of the data is given in Sec. III A concerning the substrate and in Sec. IV B concerning the Au adsorbate.

The relation between the change in phase shift $\Delta\phi$ observed in the holographic images and the corresponding thickness d of the observed object can be derived from scattering theory²¹ and is expressed via the standard formula

$$d = \frac{\Delta\phi}{V_0 C_E}, \quad (1)$$

where the interaction constant depends on the acceleration voltage resulting in $C_E = 7.29 \times 10^6 \text{ rad}/(\text{V m})$ in our case and where V_0 denotes the effective internal potential of the sample.

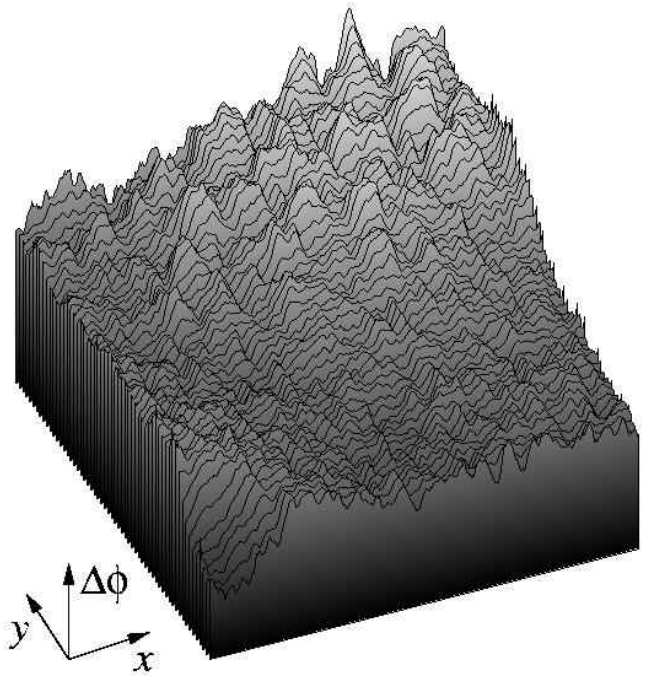


FIG. 2: (Color online) Holographic phase shift $\Delta\phi$ of a segment of the a-C substrate with part of an island as shown in Fig. 1(b) in the far right corner. The image has the size of $28.2 \times 28.2 \text{ nm}^2$. The z -axis value is proportional to the observed phase shift. In the foreground the almost linear decrease of the a-C film thickness towards its edge is visible. (For alternative representations of the data see Figs. 5 and 6.)

For bulk gold the theoretical values^{33,34} for V_0 are $V_{\text{Au, theo}} = 28 \pm 2 \text{ V}$ while experimental values³⁵ are given as $V_{\text{Au, exp}} = 22 \pm 1 \text{ V}$. For small Au clusters on TiO_2 substrates a sharp increase of V_0 for clusters smaller than 4 nm with values of up to $V_{\text{Au, cluster}} \sim 50 \text{ V}$ for clusters smaller than 2 nm.¹⁰ We confirm these findings in Sec. IV B.

For the a-C substrate films the situation is less consistent. We observe phase shifts of the substrate film with respect to the vacuum of $\sim 1.9 - 2.8$ radians. Associating these phase shifts with the numbers of the manufacturer for the film thickness of 9.5 to 14 nm we obtain a potential of $V_{\text{subs}} = 27.4 \text{ V}$.

On the other hand, the experimental value for a-C films of the same density as ours has been given by Harscher and Lichte³⁶ as $V_{\text{HL}} = 10.7 \text{ V}$. This number compares satisfactorily with the values for graphite summarized by Sánchez and Ochando³⁷ of $V_{\text{graph, theo}} \sim 12 - 15 \text{ V}$ (theory) and $V_{\text{graph, exp}} \sim 11 - 13 \text{ V}$ (experiment) since the ratio of the potentials $V_{\text{HL}}/V_{\text{graph}} \approx \rho_{\text{subs}}/\rho_{\text{graph}}$ corresponds roughly to that of the densities, i.e., the inner potential scales roughly with the density of the material. A similar argument holds for the values for diamond, where $V_{\text{dia, theo}} \sim 16 - 23 \text{ V}$ (theory) and $V_{\text{dia, exp}} \sim 15 - 21 \text{ V}$ (experiment).

The obvious discrepancy between the values of V_{subs} and V_{HL} cannot be resolved here. Possible origins of the

discrepancies are (i) the underestimation of the substrate thickness by the manufacturer^{38,39} and (ii) an increase of the internal potential for thin films similar to the increase of the internal potential in small Au clusters.¹⁰ Note that the latter effects would not have been observed for the thicker films with $d \geq 35$ nm in the investigations by Harscher and Lichte.³⁶ We will discuss the implications of the discrepancy for the present work where appropriate.

C. Density functional theory calculations

We have calculated the interaction between Au atoms and the carbon substrate using first principles DFT calculations in the generalized gradient approximation (GGA).⁴⁰ For all calculations we used the highly accurate Projector Augmented Wave method⁴¹ as implemented in the VASP electronic structure program.⁴²

For the carbon substrate we used both a graphite surface as well as a model a-C surface consisting of 150 carbon atoms. The Au-substrate interaction was calculated for a number of different positions of an Au atom relative to the substrate surface. For each position the Au-substrate interaction was mapped out by holding a Au atom fixed at different heights above the surface while the carbon atoms at and near the surface were allowed to fully relax. The resulting Au-substrate potentials were averaged and fitted to a modified Lennard-Jones potential and used as input in MC simulations described in the next section.

D. Monte-Carlo (MC) simulations

In order to develop a microscopic understanding of the dynamics of the Au clusters on the substrate we simulate the system with the canonical Monte-Carlo method. A standard Metropolis algorithm is employed^{43,44,45} with an update after each random displacement of an Au atom within an interval $[0, d_{\max}]$ in all spatial dimensions. d_{\max} is set to yield an MC acceptance rate of 50 to 60 %. The resulting temperature dependence is roughly $d_{\max} \propto \sqrt{T}$. The boundary conditions are imposed by a hard wall cube with linear dimension L_x , L_y , and L_z .

The Au-Au interaction is modeled via the many-body Gupta potential⁴⁶ (GP):

$$V(\{r_{ij}\}) = \sum_i^N \sum_{j \neq i}^N A e^{-p(r_{ij}/r_0-1)} - \sum_i^N \sqrt{\sum_{j \neq i}^N \xi^2 e^{-2q(r_{ij}/r_0-1)}}. \quad (2)$$

The distances $r_{ij} = |\mathbf{r}_i - \mathbf{r}_j|$ are measured in units of the bulk first-neighbor distance $r_0 = 2.885$ Å. The indices $i, j \in \{1, \dots, N\}$ label the Au atoms at positions \mathbf{r}_i and \mathbf{r}_j , respectively. The parameterizations for Au as found in the literature,⁴⁷ i.e., $A = 0.2061$ eV, $\xi = 1.790$ eV,

$p = 10.229$, and $q = 4.036$, has been determined to match the bulk elastic constants and the surface contraction.

The Au-substrate interaction is modeled by two-particle interactions in the form of generalized Lennard-Jones 6-12 and 3-6 potentials. Their derivation is discussed in detail in Sec. III B.

Runs on the atomic level have been performed for up to 10^8 updates per atom for up to 600 atoms. The run times on standard PCs is up to several days. Runs have been stopped when a metastable configuration is obtained that does not evolve anymore on a reasonably accessible time scale.

In order to simulate larger systems with many clusters we derive in Sec. V A an effective cluster-cluster potential. Runs are then performed with a few hundred clusters to illustrate the cluster diffusion and fusion process in Sec. V C.

III. SUBSTRATE CHARACTERIZATION

The observed formation of the islands as shown in Fig. 1 implies that the substrate surface is free of strong pinning centers. The same conclusion can be drawn from oval shapes of the islands with smooth boundaries. Moreover, the pattern formation of the Au film discussed in Sec. IV A [Fig. 1(c)] strongly suggest the presence of smooth areas on the substrate surface.

Since this observation is not ad hoc intuitive for an amorphous substrate we investigated the substrate with off-axis holography experiments. In order to obtain a qualitative understanding of the underlying mechanisms of the island formation we determine the substrate-adsorbate interactions via DFT calculations. The latter are used as input parameters for MC simulations which reproduce the experimental observations.

A. Holography

When imaging vacuum with TEM off-axis holography the phase shift observed is slightly fluctuating due to imperfections of the biprism wire, aperture, and noise induced by the CCD camera.²² We analyzed these vacuum fluctuations in order to distinguish them from the sample signal. The inset in Fig. 3(a) shows a typical image of the vacuum phase shift ϕ_{vac} after subtraction of its mean value. The main graph of Fig. 3(a) shows the normalized distribution $w_{\text{vac}}(\Delta\phi_{\text{vac}})$ of the vacuum fluctuations $\Delta\phi_{\text{vac}} = \phi_{\text{vac}}$. The full line is a Gaussian fit

$$w(\Delta\phi) = \frac{1}{\sqrt{2\pi}\sigma} \exp\left\{-\frac{(\Delta\phi)^2}{2\sigma^2}\right\} \quad (3)$$

from which we obtain a width of the vacuum fluctuations of $\sigma = \sigma_{\text{vac}} = 0.052$ rad.

The histogram in Fig. 3(b) shows the normalized phase shift distribution of the a-C substrate film *without* Au adsorbate. The Gaussian fit from Eq. 3 as shown by the full

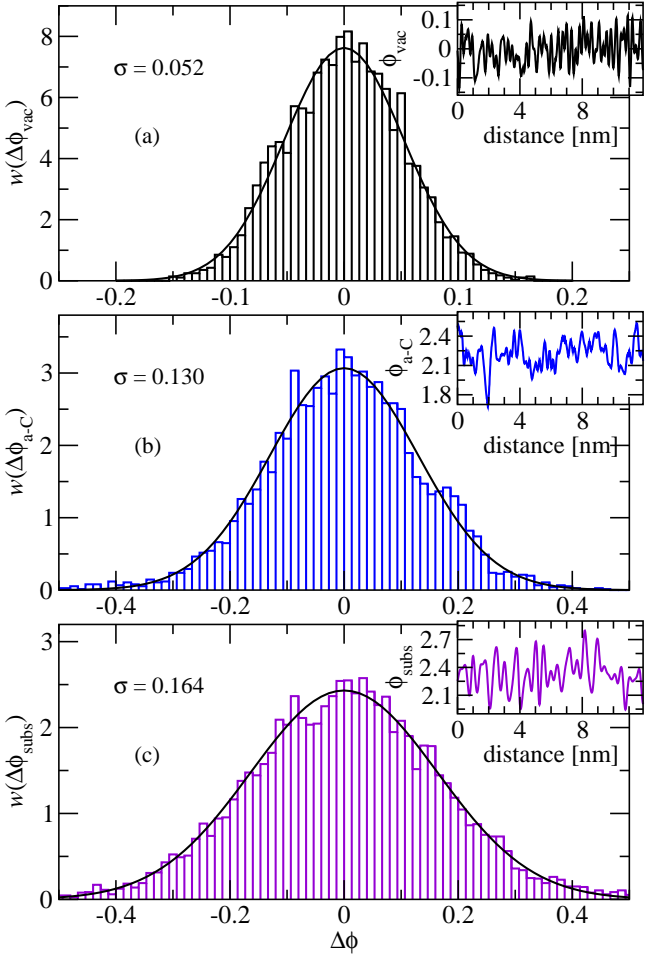


FIG. 3: (Color online) Phase shift distributions as a measure of fluctuations of the phase. Panel (a) shows the result for the vacuum, panel (b) shows the substrate film without adsorbate, and panel (c) shows the distribution for the substrate film with Au adsorbate albeit at positions without islands. Please note the different scales of the x axes. Histograms are obtained by binning and normalization of the shifted raw data, full lines are Gaussian fits to Eq. (3). The insets show samples of the measured phase shifts. The data used to obtain the histograms amounts 5 to 10 times the data shown in the insets.

line has a width of $\sigma_{a-C} = 0.13$ rad. Since $\sigma_{a-C} > 2\sigma_{vac}$ the fluctuations must reflect properties of the substrate. Using Eq. 1 and the value of $V_{subs} = 27.4$ V the change in thickness corresponds to $\Delta d_{subs} = 2\sigma_{subs}/(C_E V_{subs}) = 1.3$ nm, for $V_{HL} = 10.7$ V even $\Delta d_{subs} = 3.3$ nm. The graph in the inset Fig. 3(b) reveals that phase fluctuations of comparable depth occur on length scales of 0.3 nm. Such narrow intrusions with a depth of up to 1/5 of the substrate thickness would make the substrate very unstable. Moreover, the edges of the intrusions would inevitably lead to strong pinning centers similar to those of nanopits in HOPG,^{48,49} which are inconsistent with the observed island formation.

Since the intrusions are only 2 to 4 C-C bond lengths wide, it appears likely that they are capped in the pro-

duction process thus stabilizing the structure. The intrusions are then left as voids in the film. The effective potential is strongly reduced at the position of the voids leading to the observed phase modulation. At the same time the cap yields a rather smooth surface consistent with the observed island formation. The C atoms surrounding the voids have less nearest neighbor atoms,⁵⁰ which is consistent with the measured EELS spectra²⁴ indicating largely trivalent coordination. In the absence of methods for a more precise determination of the local structure of the substrate we use this scenario as a working hypothesis.

Finally, the histogram in Fig. 3(c) shows the normalized phase shift distribution of the a-C substrate film *with* the Au adsorbate, albeit at positions without any of the observed islands. (The latter are discussed in Sec. IV B). The Gaussian fit from Eq. 3 as shown by the full line has a width of $\sigma_{subs} = 0.164$ rad which is 25% larger than σ_{a-C} . The difference is readily interpreted as induced by small Au clusters pinned at small intrusions of the substrate. Since the pinned clusters are smaller than the TEM resolution limit their diameters must be smaller 1 nm or $N < 50$ atoms.⁵¹

B. Surface adsorbate interaction: DFT calculations

A quantitative description of Au/a-C substrate interaction is needed for the MC simulations described in Sec. V. To this end we studied the interaction of individual Au atoms with graphite and a model a-C surface using ab-initio DFT calculations.

For the calculation of the Au/graphite-surface interaction we used a supercell consisting of 2x2 graphite unit cells in the x - y plane and 4 carbon layers in the z -direction. Calculations were performed for Au in the top, bridge, and hollow sites. The calculated binding energies are 0.065eV, 0.062eV, and 0.041eV, respectively. The Au graphite potential for Au in the top-site as a function of Au atom surface distance is shown by line “g” in Fig. 4. The result of the DFT calculations was fitted with a modified Lennard-Jones potential

$$V_{LJ,graph} = V_{LJ,0} \left(\frac{0.31}{(z/r_0 - 0.1)^6} - \frac{1.11}{(z/r_0 - 0.1)^3} \right), \quad (4)$$

where $V_{LJ,0}$ is the binding energy and $r_0 = 2.885$ Å.

For a more realistic description of the a-C substrate we have constructed a model a-C surface. To ensure that sp^2 bonding will be dominant²⁴ and to obtain a simple model consistent with the observed Au-film formation we use graphite as our starting point. We use a supercell consisting of 4x4 graphite unit cells in the x - y plane and 4 carbon layers in the z direction. Additional carbon atoms were added in localized regions but otherwise randomly inbetween the graphite planes so as to create voids consistent with the observed holographic phase fluctuations.

The resulting supercell of 150 carbon atoms was relaxed into a local minimum. Two main effects of the

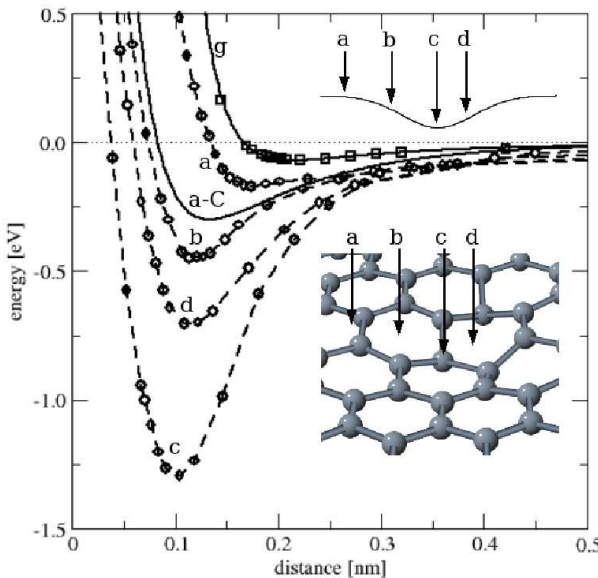


FIG. 4: (Color online) Au/graphite (squares) and Au/a-C substrate potentials (circles) as calculated within the DFT approach. The inset shows the corrugated surface layer of the a-C model with the locations of the calculated potentials (a)-(d) indicated by arrows. The fitted potentials used in the MC simulations are shown as solid lines for graphite (g) and the a-C model substrate. Dashed lines are guides to the eye.

relaxation can be observed: The carbon structure expanded strongly in the z-direction and the graphite layers buckled due to the uneven distribution of interstitial carbon atoms. The density of the final a-C model structure is $\rho \sim 2.0 \text{ g/cm}^3$ in good agreement with the density of the a-C substrate as given by the manufacturer. The surface layer of the final structure is smooth but has a corrugation of $d = 0.9 \text{ \AA}$ over a distance of a few C-C bondlengths (Fig. 4).

We have calculated the Au/a-C substrate potential at several positions roughly along a line through a depression in the surface. Since for the graphite surface the Au on top position is the preferred bonding site, only Au on top sites were considered in the a-C case. High lying C surface atoms retain their graphite character and are predominantly 3-fold coordinated. Accordingly we find the binding energy of an Au atom is still comparable to the binding energy on graphite (case a in Fig. 4). C atoms lying in a depression of the surface have additional bonds to the nearby C atoms below and are mostly 4-fold coordinated. The calculated binding energies of an Au atom to C sites lying in such a depression are considerably larger as compared to the graphite surface (cases b,d in Fig. 4). An Au atom in the center of the depression can bind to several C atoms and the binding energy is smaller but of the same order as the Au-Au binding energy (case c in Fig. 4).

To model the binding energy of Au atoms in clusters with a contact area larger than the surface intrusions the resulting Au/a-C substrate potentials were averaged

using approximate relative surface areas as weights and fitted to a modified Lennard-Jones potential

$$V_{\text{LJ,mean}} = V_{\text{LJ,0}} \left(\frac{297}{(z/r_0 - 1.2)^{12}} - \frac{34.5}{(z/r_0 - 1.2)^6} \right). \quad (5)$$

where $V_{\text{LJ,0}}$ is the binding energy and $r_0 = 2.885 \text{ \AA}$. Using weights of c:d:b:a=1:4:9:16 results in an average binding energy of $V_{\text{LJ,0}} = 0.34 \text{ eV}$. The MC simulations in Sec. V do not depend qualitatively and only little quantitatively on the specific value in a range of $0.2 < V_{\text{LJ,0}}/\text{eV} < 0.4$ and hence an average value of $V_{\text{LJ,0}} = 0.3 \text{ eV}$ was adopted.

The value of $V_{\text{LJ,0}} \sim 0.3 \text{ eV}$ is only appropriate for sufficiently large clusters. Small clusters with contact areas smaller than the intrusion size have larger weight of the strongly binding intrusion center c and are easily pinned consistent with the observations discussed in Sec. III A.

IV. LONG TIME-SCALE DYNAMICS

The long time-scale rearrangement of heavy atoms on a-C substrates has been observed previously.¹³ Here we present a detailed investigation of pattern formation of Au on a-C substrates. Figure 1(a) shows a typical TEM image of a sample prepared by deposition of 3000 shots of Au clusters on a 10 nm a-C film. The image displayed was recorded one day after the preparation of the sample. As expected, one observes a statistical particle distribution. The histogram included shows the size distribution. Au clusters smaller than 1 nm in diameter could not be discerned from the 10 nm carbon substrate background owing to their low contrast. However, ion mobility measurements have revealed⁵² that clusters in this range of sizes are widely present in cluster ion beams. This suggests that a significant number of small clusters is also present on the substrate, albeit unresolved in the TEM.

A. Island formation

After the sample is kept at room temperature and in absence of inert conditions for four months, TEM studies yield images as displayed in Fig. 1(b). The previously statistically distributed clusters are now collected in agglomerates referred to as islands. The vast majority of these islands is of similar size with typical areas of $A \sim 25 \times 70 \text{ nm}^2$.

In all islands an underlying area of higher contrast is observed, which is bordered by the outer clusters of the islands. Using EDX-detection no elements except for Au and C are found in these islands. The binary alloy phase diagram of Au and C excludes the formation of Au-C alloys under the given conditions⁵³ and we conclude the the C signature stems from the substrate. The analysis given in Secs. IV B, IV C, and IV D consistently suggest that the islands are formed of 4 to 8 monolayers of Au

on top of the substrate. This conclusion is supported by the MC simulations of the formation process of such an Au film in Sec. V.

HRTEM images of the islands as depicted in Fig. 1(c) show regions, in which crystalline patterns occur with lattice spacings determined as 500 pm and 310 pm within an estimated error of $\pm 5\%$. The angles between these two spacings differ up to 6° from a rectangular configuration. It cannot be excluded that much larger areas of the Au films are crystallized forming such patterns because a slight corrugation of the substrate may obscure its detection with HRTEM.

While the exact determination of the origin of the aforementioned patterns from the present data is not possible, it can be speculated that the Au film exhibits a similar reconstruction as has been observed for Au(111) surfaces by scanning tunneling microscopy (STM) measurements,^{54,55} where superstructures with a similar modulation⁵⁶ ($\sqrt{3} \times$ lattice constant ≈ 500 pm) have been observed. The presence of Au(111) surfaces is also consistent with the MC simulations (Sec. V). Moreover, reconstruction pattern have been observed for small islands of Au monolayers on HOPG in ultra high vacuum (UHV) by STM measurements,⁵⁷ but a direct comparison is difficult because of the larger film thickness in our samples (Sec. IV B).

We conclude that the higher contrast areas underlying the islands consist of a few monolayers of Au that form crystalline structures on at least parts of the substrate surface, which in turn must be sufficiently smooth.

B. Au-film characterization

In order to get information about the thickness of the observed films, we performed off-axis holography experiments. A three dimensional visualization of a segment of the substrate including a part of an Au island has been shown in Fig. 2 in Sec. II B. Figure 5 shows the same segment as an intensity plot, where lighter shades of gray correspond to larger phase shifts. The thick lines correspond to different scans investigated in detail. The circled areas indicate the positions of clusters adsorbed on the Au films that have been studied closely.

The results for the three scans are qualitatively equivalent and for simplicity we focus the presentation on scan 1. Figure 6(a) shows the corresponding phase profile. Four regions are clearly distinguishable from right to left: the rise of the substrate edge, the plateau of the substrate film, the rise of the Au-film edge, and finally the Au-film. The dashed lines show the profile after averaging the phase fluctuations. The vacuum level was determined in a larger area a bit further away from the sample (not shown). For the substrate edge the dashed line is a quadratic fit, for the Au-film edge it is a linear fit. The substrate plateau is given by a horizontal line at the average value of phase in that region. Finally, the Au-film base line is obtained by adapting the average value of the fluctuation phase without the adsorbed clusters as

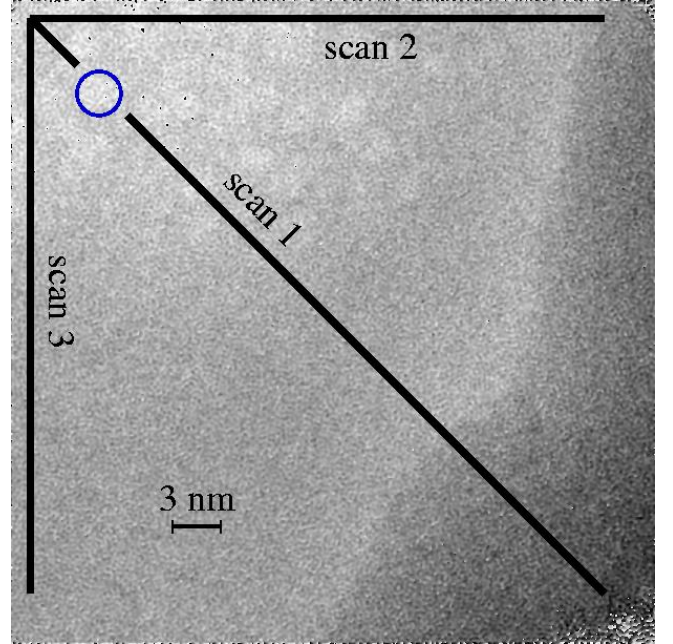


FIG. 5: (Color online) Holographic phase reconstruction image from the same segment as shown in Fig. 2 as an intensity plot. Lighter shades of gray correspond to larger phase shifts with respect to the vacuum. Lines show scans that underwent closer investigation, circles indicate the positions of selected adsorbed clusters.

outlined closer below.

Panel (b) of Fig. 6 shows the fluctuation of the data after subtraction of the dashed lines shown in panel (a). The black bar labelled “C1” indicates the position of the corresponding cluster as shown in Fig. 5.

The lower panels of Fig. 6 show the histograms of the phase distribution in panel (b) for the Au film (c), the Au-film edge (d), the substrate (e), and the substrate edge (f). The full lines are Gaussian fits from Eq. (3) except for panel (c), where a double Gaussian of the form

$$w_{\text{tot}}(\Delta\phi) = a_{\text{Au}} w_{\text{film}}(\Delta\phi) + (1 - a_{\text{Au}}) w_{\text{clus}}(\Delta\phi) \quad (6)$$

with Gaussian contributions from the film w_{film} and the adsorbed clusters w_{clus} was used. The width of the curve for the substrate of $\sigma_{\text{subs}} = 0.18$ rad is consistent with the averaged value obtained for a number of samples $\sigma_{\text{subs}} = 0.164$ as discussed in Sec. III A. The difference may be attributed to poorer statistics of the relatively small sample size in Fig. 5 and possibly to an increased number of pinned Au clusters near the islands.

The distribution for the substrate edge $\sigma_{\text{subs-edge}} = 0.24$ [Fig. 5(f)] is 30% broader as a consequence of steps and other deviations from the applied quadratic fit. The width of the phase distribution of the Au-film edge $\sigma_{\text{Au-edge}} = 0.16$ in panel (d) is close to the average value of the substrate, no smoothing of the surface corrugation is measurable. This result is consistent with the previously discussed interpretation (Sec. III A), that the phase fluctuations of the substrate stem predominantly from intrinsic spatial density inhomogeneities.

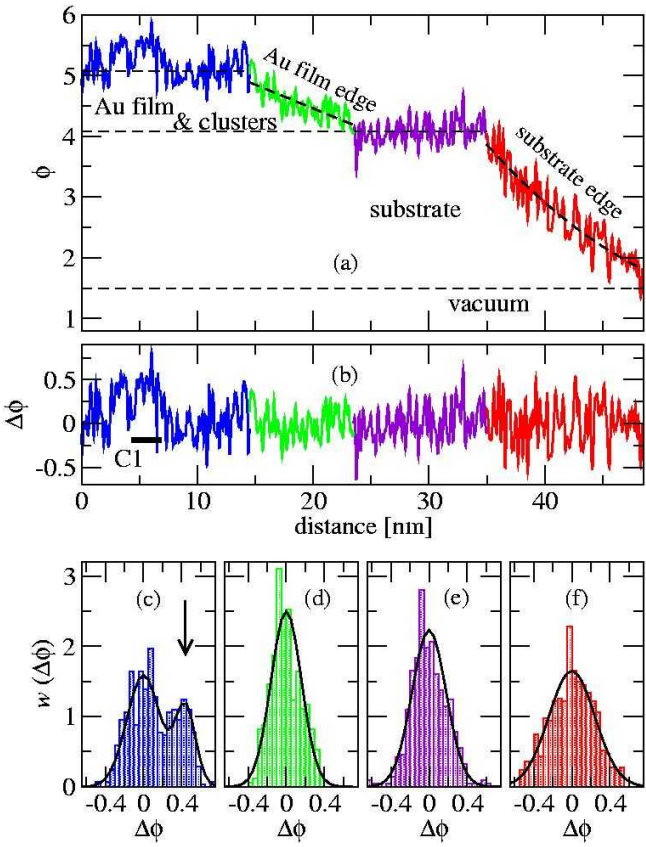


FIG. 6: (Color online) Details of scan 1 in Fig. 5. Panel (a) shows the raw data of the phase shifts together with fitted values (dashed lines, see text), which average the fluctuations. Panel (b) shows the fluctuations $\Delta\phi$ obtained from the raw data after subtraction of the fits. Panels (c), (d), (e), and (f) show the binned data of the phase fluctuations from the Au film, the Au-film edge, the substrate, and the substrate edge, respectively. Solid lines are fits from Eqs. (6) and (3).

Finally, the bimodal distribution of the Au film in panel (c) of Fig. 6 reflects the presence of adsorbed clusters on the substrate with an average height in this segment resulting in an additional phase shift of $\Delta\phi_{\text{clus}} \approx 0.43$ rad as indicated by the arrow. The width of the film part of the distribution $\sigma_{\text{film}} = 0.175$ rad is comparable to that of the substrate and stems from the intrinsic spatial density inhomogeneities of the latter. For completeness we note the values of the cluster distribution width $\sigma_{\text{clus}} = 0.11$ rad and the weighing factor $a_{\text{Au}} = 0.695$.

C. Au-film thickness

In principle the thickness of the Au film can be obtained from Eq. (1). As discussed in Sec. II B the parameter of the mean inner potential V_0 is not well defined as it appears to become thickness dependent for thin samples. To be specific, Ichikawa and coworkers¹⁰ found for Au clusters on a TiO_2 substrate with diameters smaller than 4 nm an increase of V_0 of up to a factor of 3. In

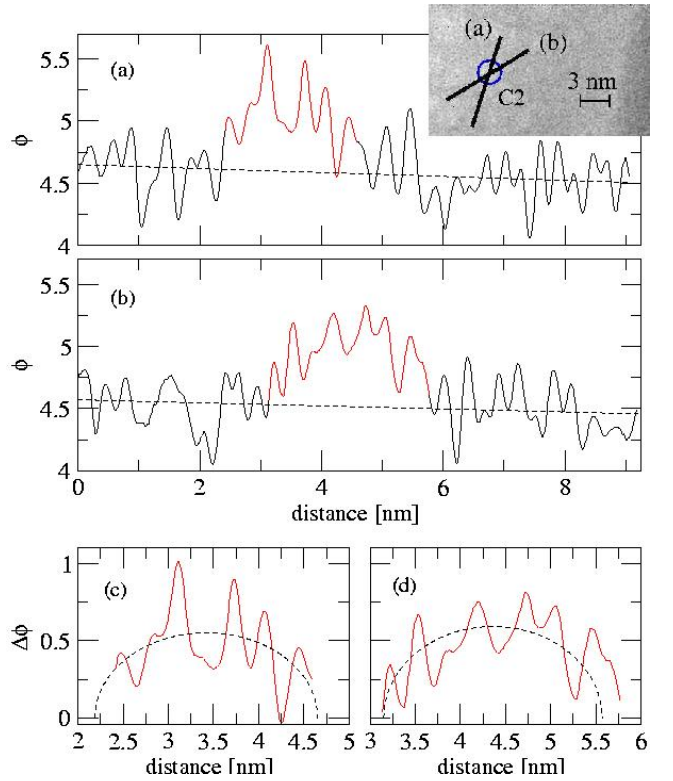


FIG. 7: (Color online) Phase shift for two scans (a) and (b) through cluster “C2” in Fig. 5 along the directions indicated in the inset. Dashed lines are linear fits to the background. Panels (c) and (d) show the data of the cluster from panels (a) and (b), respectively, after background subtraction. Dashed lines in (c) and (d) are elliptical fits (see text).

order to have a reference point for our system we have investigated the observed phase shifts of the cluster labelled with “C2” in Fig. 5 and compared the results with the shape of a cluster of the same size obtained in the MC simulations described in Sec. V B.

Panels (a) and (b) of Fig. 7 shows the resulting phase shift profiles as obtained along the scans indicated in the inset. Dashed lines are linear fits. Panels (c) and (d) show the phase profiles of the cluster after subtraction of the linear contributions together with fitted ellipses (dashed lines). As a result of the strong fluctuations the fits are not unique. A width of $b_{\text{clus}} = 2.3 \pm 0.2$ nm can be extracted while the phase shift is determined as $\Delta\phi_{\text{clus}} = 0.5 \pm 0.02$ rad. Comparing these values to the aspect ratio of $h_{\text{clus}}/b_{\text{clus}} \approx 0.54$ as obtained in Sec. V B a height of $h_{\text{clus}} = 1.2 \pm 0.1$ nm is expected. Using Eq. 1 we obtain a mean inner potential of $V_0 = 57 \pm 5$ V consistent with the results from Ichikawa *et al.*¹⁰

We have consequently confirmed the thickness dependence of the mean inner potential of Au clusters smaller than 4 nm in height. Unfortunately, when approximating the apparent strong increase of the inner potential with decreasing thickness¹⁰ in leading order as $V_0 \sim d^{-1}$, the phase shift $\Delta\phi \propto V_0 d$ becomes *independent* of the thickness in leading order. From the phase

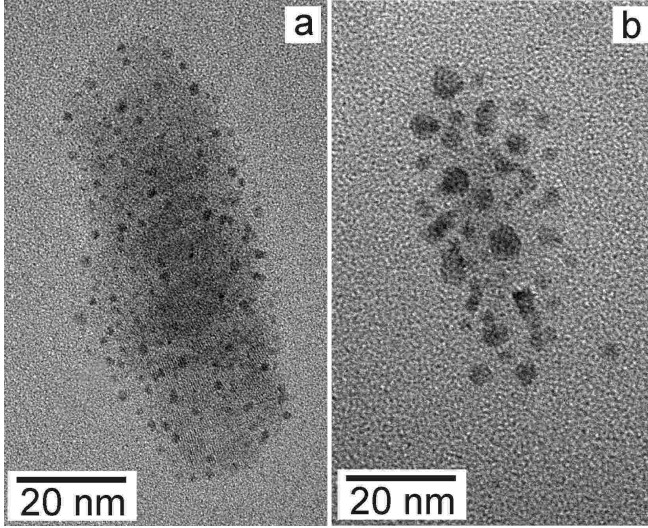


FIG. 8: (Color online) TEM images of two typical islands (a) before and (b) after *in situ* annealing at 373 K for 2 h.

shift induced by the Au film as measured in Fig. 6(a) of $\Delta\phi_{\text{film}} = \phi_{\text{film}} - \phi_{\text{subs}} \approx 1$ rad we can thus only determine an upper bound for the thickness of the Au film of $d_{\text{film}} < 7$ nm. This upper bound is obtained from Eq. (1) using the bulk value³⁵ $V_{\text{Au,exp}} \approx 22$ V, which is a lower bound for the inner potential. A more precise determination requires the detailed knowledge of the sub-leading contributions to $V_0(d)$.

The intensity profiles in Figs. 1(b) and 8(a) suggest that the film is thinner than the majority of the adsorbed clusters. This leads to an estimate of $d_{\text{film}} \sim 4 - 8$ monolayers. The observation discussed in Sec. V that clusters of size $N < 300$ (or $d_{\text{cluster}} < 2$ nm) are not stable enough to retain their structure on the substrate at room temperature and should consequently largely contribute to the film formation is consistent with these numbers.

D. Heating effects

The effects of heating on the shape of metal clusters has been studied early on.^{14,58} In order to obtain information about the stability of the islands we performed experiments heating the sample *in situ*. The sample was kept at 373 K for two hours. Figure 8(a) displays the characteristics of a typical island before heating, whereas another island, which was not exposed to the electron beam during annealing, is shown in Fig. 8(b). Comparing these two images, it is obvious that as a consequence of the heating (i) the amount of Au forming the film is diminished, (ii) the number of particles is reduced and (iii) the sizes of the remaining particles have increased.

The effects (ii) and (iii) are typical characteristics of Ostwald-ripening processes.¹¹ The islands are metastable with an activation energy low enough that the applied heating of 100 K above room temperature is sufficient to

induce the transition on a time scale of a few hours. A more elaborate investigation of the dynamical behavior of the Au islands at elevated temperatures requires more experimental data and will be presented in a subsequent publication.

V. MONTE CARLO SIMULATIONS

In order to obtain a more microscopical understanding of the formation of the Au islands—which cannot be resolved experimentally—we performed MC simulations based on the Au-substrate interaction elaborated in Sec. III and using the Gupta many-body effective potentials Eq. (2) as described in Sec. II D.

A. Cluster fusion and effective cluster potential

As discussed in Sec. IV A the observed Au film is likely to be composed of fused small Au clusters, which are present at the time of deposition but only unambiguously resolved in TEM for diameters larger than 1 nm (c.f. Fig. 1). The fusion process of adsorbed clusters has been observed experimentally for Co clusters⁴ of diameter 8.5 nm as well as for clusters⁵ of Au₅₀₀₀ and has been modeled for free clusters with MD methods using embedded atom⁵⁹ and glue potentials⁶⁰ for Au₂₂₅ to Au₃₈₀₅. The objective here is to obtain an effective inter-cluster potential in the framework of the better suited many body Gupta potentials Eq. (2), which we will use in Sec. V C to simulate the island formation.

DFT results⁶¹ show that the icosahedral configuration has a lower cohesive energy than the octahedral or cuboctahedral structures for the atomic closed shell cluster sizes $N = 13, 55, 147$. On the other hand, the Gupta potentials for Au exhibit a large number of local minima with amorphous structures and energies of $\Delta E_{55} \sim 0.01$ eV lower than the icosahedral configuration.⁶² Since $\Delta E_{55} \sim 0.01$ eV $< k_{\text{B}}T_{\text{room}} = 0.0256$ eV, we use icosahedral configurations for the investigations presented here because different isomers are realized through thermal fluctuations at room temperature.⁶³ Note that only quantitative details depend on the specific structure while our results are qualitatively quite general.

Figure 9 shows the inter-cluster cohesive energy as a function of the distance of the center of mass points r of the two clusters. Panels (a) and (b) were obtained for two Au₅₅ and two Au₁₄₇ clusters, respectively. The gray points are obtained in free MC annealing runs at room temperature ($k_{\text{B}}T = 0.0256$ eV) while the black circles were obtained at $k_{\text{B}}T = 0.0001$ eV ($T = 11.6$ K). The scattering of the gray data points reflects the thermal activation of the clusters. At low temperatures the fusion process is halted at larger distances than at room temperature because the potential energy barrier involved in the reconstruction cannot be overcome.

The full lines in Figs. 9(a) and (b) are fits representing the effective inter-cluster cohesive energy and have the

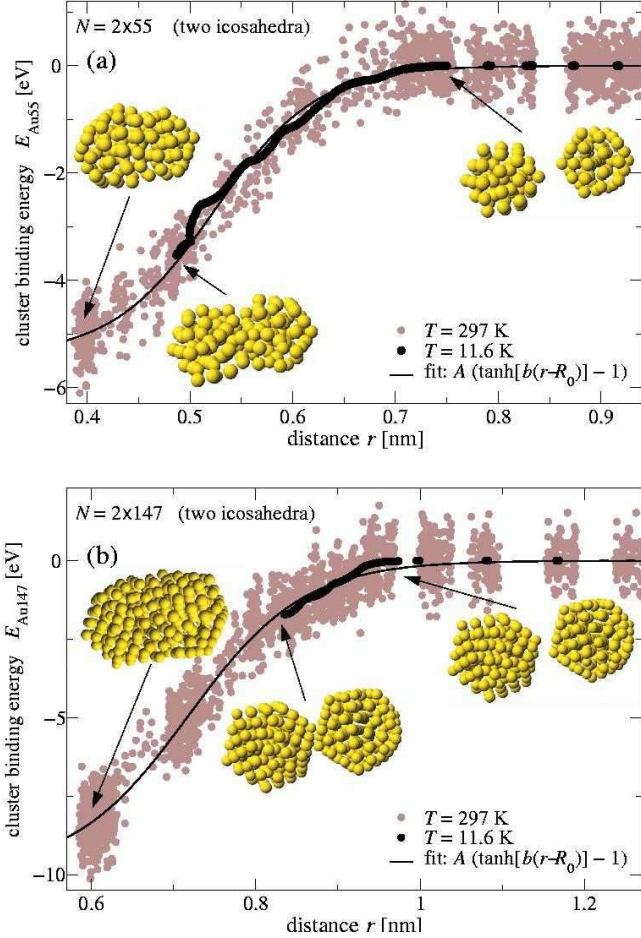


FIG. 9: (Color online) Fusion of Au_N clusters for (a) $N = 55$ and (b) $N = 147$. Gray and black circles are obtained in MC annealing runs at $k_B T = 0.0256$ eV ($T = 297$ K) and $k_B T = 0.0001$ eV ($T = 11.6$ K), respectively. The full lines are fits for the effective inter-cluster cohesive potentials Eq. (7). At low temperatures the fusion process comes to an early halt because the energy barrier involved in the atomic rearrangement cannot be overcome.

form

$$E_{AuN} = A_N \{ \tanh [b_N(r - R_{0,N})] - 1 \} . \quad (7)$$

The parameters extracted are $A_{55} = 2.702$ eV, $b_{55} = 10.08 \text{ nm}^{-1}$, $R_{0,55} = 0.524$ nm and $A_{147} = 4.941$ eV, $b_{147} = 7.149 \text{ nm}^{-1}$, $R_{0,147} = 0.718$ nm. The fusion process stops at a temperature dependent minimal distance $R_{\min,N}(T)$ which can be modeled in the potential as a step function with a high repulsive value for $r < R_{\min,N}(T)$, i.e., $E_{\text{rep}} = A_{\text{rep}} \theta[R_{\min,N}(T) - r]$ with $A_{\text{rep}} \gg A_N$. The effective binding energy is then given by $E_{\text{eff}} = E_{AuN} + E_{\text{rep}}$. In the case of the investigated icosahedral structure the values are $R_{\min,55}(T_{\text{room}}) \approx 0.4$ nm and $R_{\min,147}(T_{\text{room}}) \approx 0.6$ nm. Note that larger clusters are structurally more stable than smaller clusters and consequently the fusion process at $k_B T = 0.0001$ eV ($T = 11.6$ K) leaves the initial structure of the two Au_{147} clusters more intact [Fig. 9(b)] than in the case of two

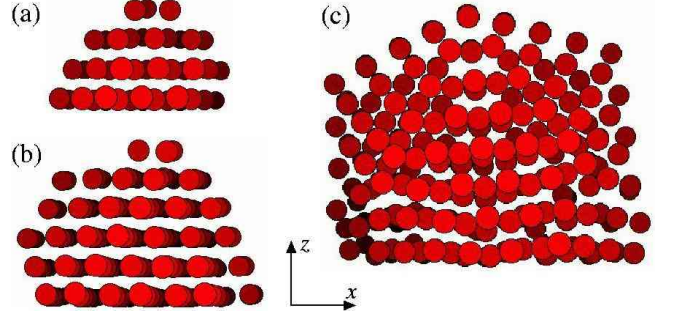


FIG. 10: (Color online) Side view of the shape of adsorbed clusters of size (a) $N = 55$, (b) $N = 147$, and (c) $N = 309$. The initially icosahedral clusters are placed on a planar substrate in the x - y plane modeled with a generalized Lennard-Jones potential Eq. 5 with a depth of the minimum of $V_{LJ,0} = -0.3$ eV and simulated at room temperature ($k_B T = 0.0256$ eV). The clusters are reconstructed in hcp (a), fcc (b), and distorted icosahedral (c) structures as a consequence of the boundary condition imposed by the substrate. (The images were taken after quenching to $T = 11.6$ K in order to eliminate noise.)

Au_{55} clusters [Fig. 9(a)].

B. Shape and adsorption energy of the adsorbed clusters

For the interpretation of the holographic analysis of the Au film and the Au clusters it is useful to have information about their shape. Moreover, from the simulations we obtain the effective attractive potential of the substrate exerted onto clusters of different size.

1. Amorphous carbon substrate

Since the exact shape of the substrate surface is not known (c.f. discussion in Sec. III) we simulate the shape of clusters for flat surfaces with different relevant effective mean substrate-adsorbate potentials derived in Sec. III B. Figure 10 shows a side view the shape of adsorbed clusters (substrate at the bottom) in the presence of a flat substrate with an attractive potential as given by Eq. 5 with a depth of $V_{LJ,0} = 0.3$ eV. The clusters of size (a) $N = 55$, (b) $N = 147$, and (c) $N = 309$ were prepared in icosahedral configurations close to the surface and subsequently freely evolved in a simulation run at room temperature ($k_B T = 0.0256$ eV) for 10^7 to 10^8 Monte Carlo steps per atom.

As a result of the boundary condition imposed by the substrate the clusters reconstructed in the simulation process to hcp (a), fcc (b), and distorted icosahedral (c) structures. As expected, the larger $N = 309$ cluster is more stable than the smaller ones and does not undergo a structural transition within reasonable run times. The energy gain due to the Au-substrate interaction is roughly the number of atoms at the surface

times the potential depth $V_{\text{LJ},0}$. To be specific, we find $\Delta E_{\text{subs},55} = -6.31$ eV, $\Delta E_{\text{subs},147} = -10.85$ eV, and $\Delta E_{\text{subs},309} = -12.02$ eV for the configurations shown in Fig. 10 as compared to the icosahedral structures.

When briefly tempering the clusters with $N = 55$ and $N = 147$ at $k_B T \sim 0.7$ eV and subsequent quenching we find that both hcp and fcc structures are realized. The energy differences of the hcp configuration with respect to the bulk-ground-state fcc structure is smaller than energy fluctuations due to boundary effects. This observation is consistent with the frequently observed⁶⁴ stacking faults in fcc and hcp bulk crystals.

For completeness we have performed runs simulating a graphite substrate using Eq. (4) with a potential depth of $V_{\text{LJ},0} = 0.09$ eV. We find that Au_{55} is amorphous at room temperature while Au_{147} retains its initial icosahedral structure (not shown). The melting point⁴⁵ of Au_{55} in the absence of the substrate is close to room temperature,^{65,66,67,68,69} which accounts for its larger sensitivity to boundary effects.

2. Gold film

When placing a number of randomly distributed Au atoms on the homogeneous substrate as described by Eq. (5) a hexagonally coordinated double layer is found to be the metastable structure attained (see also Sec. V D) for a large parameter range of $0.1 < V_{\text{LJ},0}/\text{eV} < 0.6$. The surface of such an Au double layer corresponds to an Au(111) surface, albeit with 3.5% contracted nearest-neighbor bond-length due to surface effects.⁴⁶ In order to model the shape of the Au clusters that are found on the Au film we placed an initially icosahedral cluster $N = 309$ on the substrate surrounded by such an Au double layer formed of 291 atoms. The diameter of such a cluster of $d \approx 2.1$ nm corresponds to that investigated in Sec. IV C.

Figure 11 shows the resulting shape of the cluster from the side in panel (a) and from the top in panel (b). Since the Au-double-layer-cluster interaction is much stronger than the substrate-cluster interaction [c.f. Fig. 10(c)], the cluster completely reconstructs to an fcc lattice to match the structure of the film.

C. Island formation

In order to model the formation of the islands on the a-C substrate we simulate the dynamics of clusters rather than individual atoms, which allows us to model sufficiently large systems. Moreover, we are able to reproduce experimental results^{4,5,6} for the diffusion and agglomeration of size selected clusters published previously.

In Sec. IV C we have shown from the experimental holographic data that the Au film in the islands is less than 7 nm. In Sec. V B the MC simulations have shown that small adsorbed clusters of Au_N for $N = 55$ and

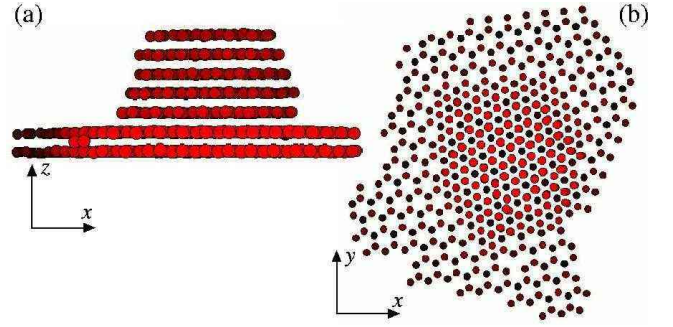


FIG. 11: (Color online) Side (a) and top (b) view of an Au_{309} cluster surrounded by an Au double layer bound to a substrate as modeled by Eq. (5) with $V_{\text{LJ},0} = 0.3$ eV at room temperature ($k_B T = 0.0256$ eV). The Au_{309} was initially icosahedral but reconstructed to a fcc lattice under the influence of the Au(111) double layer. (The images were taken after quenching to $T = 11.6$ K in order to eliminate noise.)

$N = 147$ do not retain their structure at room temperature and can easily fuse. Smaller clusters are more likely to be trapped by pinning centers on the corrugated a-C film as discussed in Secs. III A and III B, while larger clusters are more stable and retain their structure instead of fusing with their environment as indicated in Secs. V A and V B. These findings suggest that the Au films of the islands are formed by diffusing and coalescing clusters on the substrate in the size range around $50 < N < 300$ leading to a film thickness of 4 to 8 monolayers.

For simplicity we show here simulations of a system with an effective cluster cohesive potential of the form given by Eq. (7) with parameters as obtained for $N = 147$. Correspondingly, the cluster-substrate attractive potential is given by Eq. (5), where we use a value of $V_{\text{LJ},0} = 11$ eV as obtained from the quantitative analysis in Sec. V B. Results obtained for parameters with $N = 55$ are qualitatively equivalent (not shown).

Figure 12 shows a series of snapshots⁷⁰ from a simulation run of 200 initially randomly placed effective Au_{147} clusters. Panel (a) shows that after 3000 MC steps per cluster small islands and chains of clusters have formed very similar to those observed on short time scales for monodisperse 4.8 nm diameter Au clusters on an a-C substrate,⁵ Ag_{5000} clusters on graphite,⁶ and 8.5 nm diameter Co clusters on microgrid substrates.⁴ It is important to note that the time scales for the diffusion and fusion processes depend on the temperature, the substrate properties, and the cluster sizes so that these metastable structures can be observed only in a system specific time window.

At room temperature the Au_{147} clusters can be considered as to be fused almost instantaneously compared with the diffusion time scales as shown in Fig. 9(b). Correspondingly the radius of the dots representing the Au_{147} clusters in Fig. 12 has been chosen as $R_{\min,147}(T_{\text{room}}) = 0.6$ nm. Larger clusters fuse on much longer time scales or at higher temperatures.^{4,5,6,59,60} From the MC simulations a diffusion coefficient cannot be determined quan-

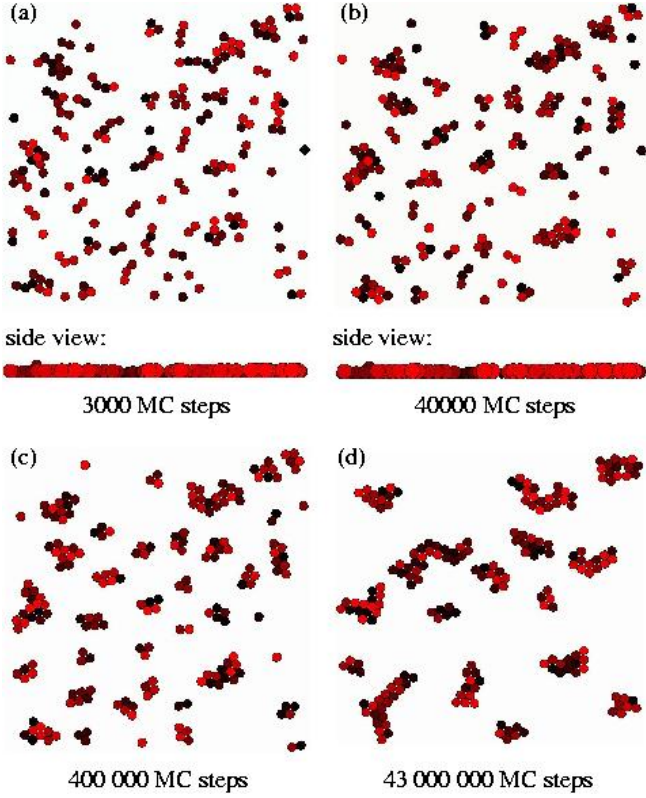


FIG. 12: (Color online) Simulation of 200 Au_{147} clusters interacting as described by Eq. (7) on a substrate modeled by Eq. (5) with $V_{\text{LJ},0} = 11$ eV after (a) 3000, (b) 4×10^4 , (c) 4×10^5 , and (d) 4.3×10^7 MC steps per cluster. The radius of the dots representing the clusters has been chosen as $R_{\min,147}(T_{\text{room}}) = 0.6$ nm, i.e., touching clusters are fused as shown in Fig. 9(b). The side views in panels (a) and (b) show that all clusters are located in a plane touching the substrate.⁷⁰

titatively because of the lack of a time constant in the MC procedure.

Panels (b), (c) and (d) of Fig. 12 shows the system after 4×10^4 , 4×10^5 , and 4.3×10^7 MC steps per cluster, respectively. Clusters and islands of clusters coalesce once they get close enough gaining cohesive energy. Structures with short border lines are favored over extended linear ones for the same reason. The (expected) tendency to form larger islands by diffusion and fusion is clearly visible. The present simulation of effective clusters underestimates the migration speed as well as the reorganization⁵⁸ of the islands to more circular structures because the diffusion of the individual atoms on the surface of the clusters is not accounted for. For larger clusters the latter is the dominant cluster migration process^{1,71} referred to as surface diffusion. Including this effects requires the investigation of much smaller systems such as shown in Sec. V D.

In conclusion the cluster diffusion and fusion as modeled by the effective clusters and cluster interactions correctly accounts for the experimentally observed^{4,5,6} pattern formation [Fig. 12(a)]. The fused clusters [Fig. 9(b)]

form small islands [Fig. 12(d)] with a thickness of roughly the cluster diameter, which corresponds in the case of Au_{147} to 5 monolayers [Fig. 10(b)]. The expected continued migration by surface diffusion^{1,71} and fusion of the small islands in Fig. 12(d) is consistent with the experimentally observed island formation shown in Fig. 1(b).

D. Cluster drag

All initially randomly distributed larger clusters are incorporated into the Au films in the islands as shown in Figs. 1(b) and 8(a). It is not possible to simulate this effect directly because of the size limitations of the method. It is possible though to place randomly distributed Au atoms on a substrate modeled by the generalized Lennard Jones potential Eq. (5), where $V_{\text{LJ},0} = 0.3$ eV, together with a $N = 147$ and a $N = 55$ Au cluster at room temperature ($k_{\text{B}}T = 0.0256$ eV). The thus modeled system is significantly smaller than those observed in the experiments but the dynamical behavior is likely to be similar, albeit with rescaled diffusion constants and time scales.

Snapshots taken at three different run times are shown in Fig. 13. Panel (a) shows the initially random distribution of 298 atoms as well as the Au_{55} and Au_{147} clusters after 93 MC steps per atom. Panel (b) shows the system after 6×10^4 MC steps per atom. The percolating regions coalesce. Panel (c) shows a side view of the same state of the system as in (b) and illustrates that the atoms have formed a Au double layer. This double layer is stable at room temperature in a substrate parameter range of $0.1 < V_{\text{LJ},0}/\text{eV} < 0.6$.

Panel (d) of Fig. 13 shows the system after 1.18×10^6 MC steps per atom. The coalescing Au double layer has contracted thus minimizing its cohesive energy. In the cohesion process the less mobile Au_{55} and Au_{147} clusters have been pulled closer together. They are located closer to the border of the Au film consistent with the experiments indicating a slightly larger probability to find clusters near the boundaries of the islands than in their center. The separated island in the lower right hand corner of Fig. 13 is less mobile and fuses with the larger island only after comparably long run times (not shown).

Panel (e) of Fig. 13 shows a side view of the system after 1.18×10^6 MC steps per atom and illustrates the fcc restructuring of the initially icosahedral clusters in the presence of the Au double layer film.

VI. CONCLUSIONS

We presented experimental results showing the formation of Au islands on amorphous carbon substrates after laser deposition of non-size-selected clusters and subsequent aging of the samples in the absence of inert condition for three to four months. We characterized both the substrate and the Au films with electron transmission

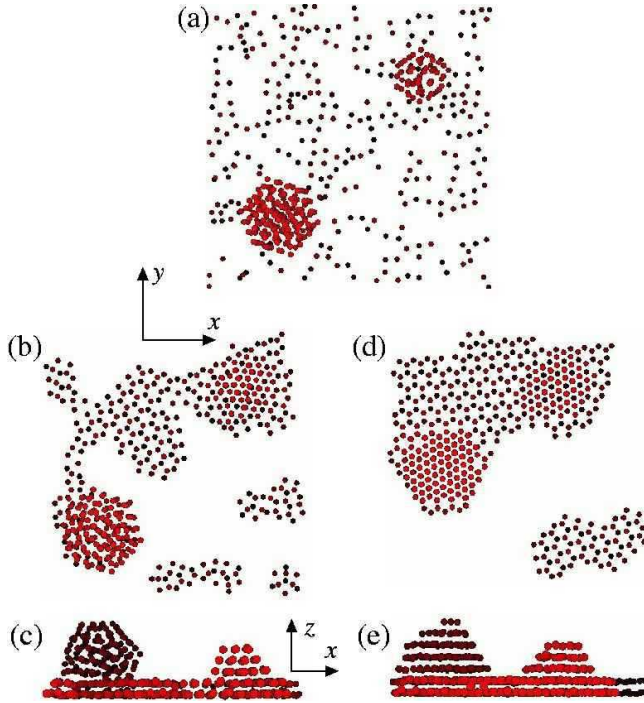


FIG. 13: (Color online) Time evolution of a system of 298 Au atoms placed randomly on the substrate [Eq. (5)] and two Au_{55} and Au_{147} clusters. Panel (a): 93 MC steps; panel (b) and (c): 6×10^4 MC steps; panel (d) and (e): 1.18×10^6 MC steps per atom. Panels (c) shows the formation of the double layer film, panel (e) the restructuring of the initially icosahedral clusters. (The images were taken after quenching to $T = 11.6$ K in order to eliminate noise.)

holography. A model potential for the substrate-Au interaction was derived with the help of density functional calculations. Subsequently a number of Monte Carlo simulations were carried out describing the island formation process and the shape of the adsorbed clusters.

The following qualitative and quantitative results have been incurred from the investigations.

- The observed islands have a typical size of $A \sim 25 \times 70 \text{ nm}^2$.
- The islands consist of an Au film of a few monolayers [probably 4 to 8 but definitely less than 27

Au(111) layers] thickness and adsorbed larger clusters.

- The islands are metastable and coalesce at elevated temperatures of $T \sim 400$ K.
- The islands are formed by diffusion and coalescence of clusters of size $50 < N < 300$.
- Larger clusters, which normally are less mobile, are dragged along by the percolating Au film formed by the smaller clusters.
- Smaller clusters are pinned at deeper substrate intrusions as indicated by the broadening of the phase distribution in the holographic images of the ablated samples.
- A number of observations suggest that the amorphous carbon substrate surface is much less corrugated than anticipated. Instead, the substrate appears to exhibit significant internal spatial density fluctuations.
- The Au-substrate interaction can be modeled by a generalized Lennard-Jones potential for graphite [Eq. (4)] and for amorphous carbon [Eq. (5)].
- An effective Au cluster-cluster interaction has been determined [Eq. (7)].

The extensive investigation presented in this work contribute to a better understanding of some processes taking place in the so far little investigated field of the dynamic behavior of cluster arrays deposited on amorphous surfaces.

Acknowledgments

We thank S.-S. Jester and M. M. Kappes for the sample preparation, outlining the preparation process, and discussions. RW thanks P. Schmitteckert, M. Vojta, and P. Wölfe for instructive discussions. The work was supported by the Center for Functional Nanostructures of the Deutsche Forschungsgemeinschaft within project area D1.

¹ P. Wynblatt and N. A. Gjostein, *Progr. Sol. State Chem.* **9**, 21 (1975).

² P. Williams, *Appl. Phys. Lett.* **50**, 1760 (1987).

³ K. Morgenstern, G. Rosenfeld, and G. Comsa, *Phys. Rev. Lett.* **76**, 2113 (1996).

⁴ D. L. Penga, T. J. Konno, K. Wakoh, T. Hihara, and K. Sumiyama, *Appl. Phys. Lett.* **78**, 1535 (2001).

⁵ D. A. Eastham, B. Hamilton, and P. M. Denby, *Nanotechnology* **13**, 51 (2002).

⁶ M. Couillard, S. Pratontep, and R. E. Palmera, *Appl.*

Phys. Lett. **82**, 2595 (2003).

⁷ M. Forshaw, R. Stadler, D. Crawley, and K. Nikolic, *Nanotechnology* **15**, 220 (2004).

⁸ G. Allan, C. Delerue, C. Krzeminski, and M. Lannooi, *Nanostruct. Mat.* 161 (2002).

⁹ A. Pestyakov, V. Lunin, A. Kharlanov, N. Bogdanchikova, and I. Tuzovskaya, *Euro. Phys. J. D* **24**, 307 (2003).

¹⁰ S. Ichikawa, T. Akita, M. Okumura, M. Kohyama, and K. Tanaka, *JEOL News* **38**, 6 (2003).

¹¹ W. Ostwald, *Z. Phys. Chem. (Leipzig)* **34**, 495 (1900).

¹² C. Wagner, *Z. Elektrochem.* **65**, 581 (1961).

¹³ M. Utlaut, *Phys. Rev. B* **22**, 4650 (1980).

¹⁴ D. J. Smith, A. K. Petford-Long, L. R. Wallenberg, and J.-O. Bovin, *Science* **233**, 872 (1986).

¹⁵ M. Y. Efremov, F. Schiettekatte, M. Zhang, E. A. Olson, A. T. Kwan, R. S. Berry, and L. H. Allen, *Phys. Rev. Lett.* **85**, 3560 (2000).

¹⁶ D. J. Wales, J. P. K. Doye, M. A. Miller, P. N. Mortenson, and T. R. Walsh, *Adv. Chem. Phys.* **115**, 1 (2000).

¹⁷ J. Hagen, L. Socaciu, U. Heiz, T. Bernhardt, and L. Wöste, *Euro. Phys. J. D* **24**, 327 (2003).

¹⁸ D. Gross, *Microcanonical thermodynamics: Phase transitions in Small systems, volume 66 of Lecture Notes in Physics* (World Scientific, Singapore, 2001).

¹⁹ K. Fauth, S. Gold, M. Heßler, N. Schneider, and G. Schütz, *Chem. Phys. Lett.* **392**, 498 (2004).

²⁰ W. Vervisch, C. Mottet, and J. Goniakowski, *Euro. Phys. J. D* **24**, 311 (2003).

²¹ L. Reimer, *Transmission electron microscopy* (Springer, Berlin, 1989).

²² M. Lehmann and H. Lichte, *Microsc. Microanal.* **8**, 447 (2002).

²³ J. Robertson, *Adv. Phys.* **35**, 317 (1986).

²⁴ B. Reznik, M. Fotouhi, and D. Gerthsen, *Carbon* **42**, 1305 (2004).

²⁵ J. T. Titantah and D. Lamoen, *Phys. Rev. B* **70**, 033101 (2004).

²⁶ P. Weis, S. Gilb, P. Gerhardt, and M. M. Kappes, *Int. J. Mass Spec.* **216**, 59 (2002).

²⁷ P. Weis, O. Welz, E. Vollmer, and M. M. Kappes, *J. Chem. Phys.* **120**, 677 (2004).

²⁸ P. Milani and W. A. deHeer, *Rev. Sci. Instrum.* **61**, 1835 (1990).

²⁹ T. G. Dietz, M. A. Duncan, D. E. Powers, and R. E. Smalley, *J. Chem. Phys.* **74**, 6511 (1981).

³⁰ U. Heiz, F. Vanolli, L. Trento, and W.-D. Schneider, *Rev. Sci. Instrum.* **68**, 1986 (1997), and references therein.

³¹ A. Rosenauer, S. Kaiser, T. Reisinger, J. Zweck, W. Gebhardt, and D. Gerthsen, *Optik* **102**, 63 (1996).

³² Since the wavelength of the electronic wave-function is longer in the sample medium than in vacuum²¹ the phase shift measured is actually negative. For a more intuitive representation, where larger values correspond to larger sample thickness, we have inverted the ϕ axes.

³³ R. Buhl, *Z. Phys.* **155**, 395 (1959).

³⁴ M. Keller, *Z. Phys.* **164**, 274 (1961).

³⁵ M. Gajdardziska-Josifovska and A. H. Carim, in *Introduction to Electron Holography*, edited by E. Voelkl, L. F. Alldard, and D. C. Joy (Plenum Press, New York and London, 1999), pp. 241–268.

³⁶ A. Harscher and H. Lichte, in *Proceedings of the 14th International Congress on Electron Microscopy*, edited by H. Calderon-Benavides and M. J. Jose-Yacaman (IOP Publishing Ltd., London, 1998), Vol. 1, p. 553.

³⁷ A. Sánchez and M. Ochando, *J. Phys. C: Solid St. Phys.* **18**, 33 (1985).

³⁸ S. M. Ritzau and R. A. Baragiola, *Phys. Rev. B* **58**, 2529 (1998).

³⁹ F. Allegrini, R. F. Wimmer-Schweingruber, P. Wurz, and P. Bochsler, *Nucl. Instr. and Meth. B* **211**, 487 (2003).

⁴⁰ Y. Wang and J. P. Perdew, *Phys. Rev. B* **44**, 13298 (1991).

⁴¹ P. E. Blöchl, *Phys. Rev. B* **50**, 17953 (1994).

⁴² G. Kresse and D. Joubert, *Phys. Rev. B* **59**, 1758 (1999).

⁴³ M. P. Allen and D. J. Tildesley, *Computer Simulation of Liquids*, *Oxford Science Publications* (Clarendon Press, Oxford, 1989).

⁴⁴ J. Wanga, F. Dinga, W. Shena, T. Lia, G. Wanga, and J. Zhaod, *Solid State Commun.* **119**, 13 (2001).

⁴⁵ R. Werner, submitted to *Eur. Phys. J. B*.

⁴⁶ R. P. Gupta, *Phys. Rev. B* **23**, 6265 (1981).

⁴⁷ F. Cleri and V. Rosato, *Phys. Rev. B* **48**, 22 (1993).

⁴⁸ H. Hövel, T. Becker, A. Bettac, B. Reihl, M. Tschudy, and E. J. Williams, *J. Appl. Phys.* **81**, 154 (1997).

⁴⁹ H. Hövel, *Appl. Phys. A* **72**, 295 (2001).

⁵⁰ J. Dong and D. A. Drabold, *Phys. Rev. B* **57**, 15591 (1998).

⁵¹ J. Urban, *Cryst. Res. Technol.* **33**, 1009 (1998).

⁵² S. Gilb, P. Weis, F. Furche, R. Ahlrichs, and M. M. Kappes, *J. Chem. Phys.* **116**, 4094 (2002).

⁵³ R. B. McLellan, *Scr. Metall.* **3**, 389 (1969).

⁵⁴ V. M. Hallmark, S. Chiang, J. F. Rabolt, J. D. Swalen, and R. J. Wilson, *Phys. Rev. Lett.* **59**, 2879 (1987).

⁵⁵ L. Huang, J. Chevrier, P. Zeppenfeld, and G. Cosma, *Appl. Phys. Lett.* **66**, 935 (1995).

⁵⁶ M. A. van Hove, R. J. Koestner, P. C. Stair, J. P. Biberian, L. L. Kesmodel, I. Bartos, and G. A. Somorjai, *Surf. Sci.* **103**, 189 (1981).

⁵⁷ E. Ganz, K. Sattler, and J. Clarke, *Phys. Rev. Lett.* **60**, 1856 (1988).

⁵⁸ M. Drechsler, J. J. Métois, and J. C. Heyraud, *Surf. Sci.* **108**, 549 (1981).

⁵⁹ L. J. Lewis, P. Jensen, and J.-L. Barrat, *Phys. Rev. B* **56**, 2248 (1997).

⁶⁰ S. Arcidiacono, N. Bieri, D. Poulikakos, and C. Grigopoulos, *Int. J. Multiph. Flow* **30**, 979 (2004).

⁶¹ O. D. Häberlen, S.-C. Chung, M. Stener, and N. Rösch, *J. Chem. Phys.* **106**, 5189 (1997).

⁶² I. L. Garzón, K. Michaelian, M. R. Beltrán, A. Posada-Amarillas, P. Ordejón, E. Artacho, D. Sánchez-Portal, and J. M. Soler, *Phys. Rev. Lett.* **81**, 1600 (1998).

⁶³ J. P. K. Doye and D. J. Wales, *Phys. Rev. Lett.* **80**, 1357 (1998).

⁶⁴ N. Chetty and M. Weinert, *Phys. Rev. B* **56**, 10844 (1997).

⁶⁵ F. Ercolelli, W. Andreoni, and E. Tosatti, *Phys. Rev. Lett.* **66**, 911 (1991).

⁶⁶ Y. G. Chushak and L. S. Bartell, *J. Phys. C* **105**, 11605 (2001).

⁶⁷ K. Koga, T. Ikeshoji, and K. I. Sugawara, *Phys. Rev. Lett.* **92**, 115507 (2004).

⁶⁸ C. L. Cleveland, W. D. Luedtke, and U. Landman, *Phys. Rev. B* **60**, 5065 (1999).

⁶⁹ R. Werner, unpublished.

⁷⁰ The color coding of Figs. 10 through 13 is such that the objects closest to the viewer are lighter and the most distant objects are dark. The color gradient is normalized to the maximum difference in distance of objects. As a result the different clusters shown in Fig. 12 appear in different shades even though they all are positioned in the same plane with very little difference in distance from the substrate, which becomes apparent in the side views in panel (a) and (b).

⁷¹ E. E. Gruber, *J. Appl. Phys.* **38**, 243 (1967).